JACS
JOURNAL OF THE AMERICAN CHEMICAL SOCIETY
Article
pubs.acs.org/JACS

Solvent-Mediated Self-Assembly of Nanocube Superlattices

Zewei Quan,[†,§] Hongwu Xu,[§] Chenyu Wang,[†] Xiaodong Wen,[∥] Yuxuan Wang,[‡] Jinlong Zhu,[⊥] Ruipeng Li,[▽] Chris J. Sheehan,[#] Zhongwu Wang,[▽] Detlef-M. Smilgies,[▽] Zhiping Luo,*[,○,◆] and Jiye Fang*[,†,‡]

[†]Department of Chemistry and [‡]Materials Science and Engineering Program, State University of New York at Binghamton, Binghamton, New York 13902, United States

[§]Earth and Environmental Sciences Division, [∥]Theoretical Division, [⊥]Los Alamos Neutron Science Center, and [#]Materials Physics and Applications Division, Los Alamos National Laboratory, Los Alamos, New Mexico 87545, United States

[▽]Cornell High Energy Synchrotron Source, Wilson Laboratory, Cornell University, Ithaca, New York 14853, United States

[○]Department of Chemistry and Physics, Fayetteville State University, Fayetteville, North Carolina 28301, United States

[◆]Microscopy and Imaging Center, Texas A&M University, College Station, Texas 77843, United States

Supporting Information

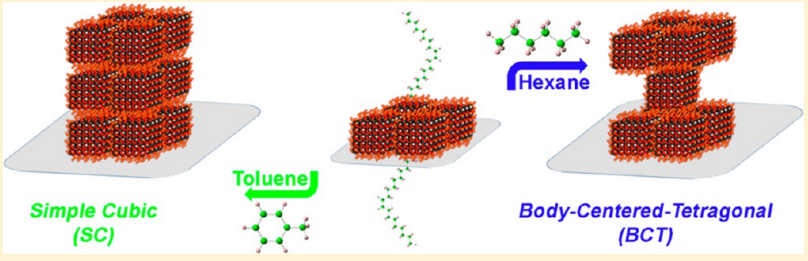

ABSTRACT: Self-organization of colloidal Pt nanocubes into two types of distinct ordered superlattices, simple-cubic and body-centered-tetragonal structures, has been achieved using a home-built setup. Detailed translational and orientational characteristics of these superstructures were determined using a transmission electron microscopy tomographic technique with 3D reconstruction analysis. The formation of these distinct superlattices is the result of a delicate choice of solvent (i.e., aliphatic hexane or aromatic toluene hydrocarbons), which serves as a dispersion medium to fine-tune the relative strengths of ligand−ligand and ligand−solvent interactions during the self-assembly process. This work provides important insights into the effects of ligand−solvent interactions on superlattice formation from nonspherical nanoparticles.

INTRODUCTION

As a result of the intricate interactions between excitons, surface plasmons, or magnetic moments of the assembled building blocks, superlattices consisting of inorganic nanoparticles (NPs) often exhibit distinct collective electronic, optical, and magnetic properties compared with the corresponding individual NPs and their bulk solid counterparts.[1−7] These intriguing characteristics have inspired the quest for further understanding and control of the self-assembly of NP superstructures, which may offer opportunities to optimize the existing material properties and discover emerging collective physical phenomena that may have potential technological applications. However, the understanding of the self-assembly processes/mechanisms of colloidal NPs is still in its infancy, as interparticle interactions such as van der Waals, electrostatic, and entropic forces in an assembly process are complex and, in many cases, interdependent.[8,9] Consequently, systematic studies of the formation of NP superstructures by carefully regulating these multiple interactions and their relative contributions are being intensively pursued.[8,10−14]

Colloidal NPs are usually coated with a layer of organic molecules, forming a stable colloidal dispersion in an adequate solvent.[15] The steric stabilization of NPs with organic ligand shells suppresses the attractive interactions between NPs (and thus random NP conglomeration), while it facilitates self-assembly of NPs into certain types of superlattices. Interactions of an NP with its neighboring particles and/or its environment (e.g., the solvent and the substrate) can be controlled via its organic ligand shell. The important role of the organic ligands in NP self-assembly processes has therefore been extensively investigated.[7,16−21] For instance, the concept of effective "softness" of an NP/ligand complex based on the ratio of ligand length to particle radius was utilized to explain the formation of unusual non-close-packed (e.g., body-centered-cubic) rather than close-packed (e.g., face-centered cubic) superstructures consisting of spherical NPs.[19,21] In addition, it was recently realized that the formation of an NP superlattice may consist of various intricate nucleation and growth steps

Received: August 9, 2013
Published: January 3, 2014

 © 2014 American Chemical Society dx.doi.org/10.1021/ja408250q | J. Am. Chem. Soc. 2014, 136, 1352−1359

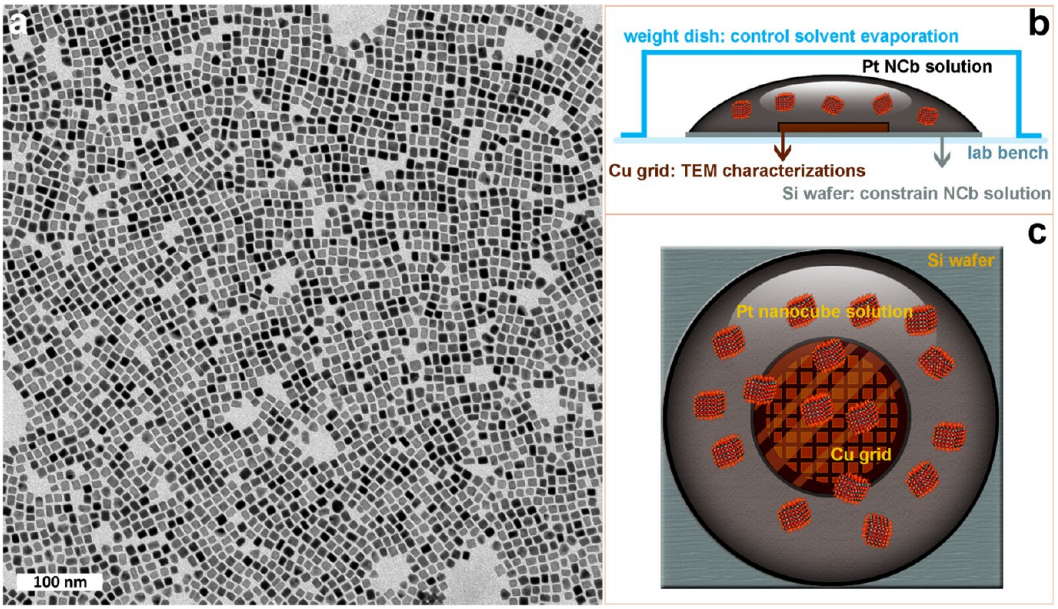

Figure 1. (a) TEM image of Pt NCbs assembled by directly drop-casting their hexane colloidal solution on a Cu TEM grid. (b, c) Schematic side and top views, respectively, of the controlled evaporation setup for assembly of Pt NCbs on a carbon-coated Cu grid.

involving multiple NP interactions associated with surface-capped ligands and surrounding solvents.[18] Moreover, single-component NPs with a modification of the strength and directionality of the ligand–ligand interactions by DNA functionalization can be directed to form different superstructures.[22] From all of these studies, it is clear that the interactions arising from the surrounding ligands can serve as an effective means for the design of self-assembled NP superstructures, potentially with desired nano/mesoscale phenomena and properties.

The ligand–ligand interactions can best be exploited using anisotropic NPs with smooth planar surfaces since such building blocks potentially have more efficient contacts on their exclusion surfaces compared with their spherical counterparts.[1,23] One typical class of anisotropic NPs is nanocubes (NCbs), which may serve as a good model system for studying ligand interactions.[20,23−29] It has actually been theoretically demonstrated that the coupling energy between cubic NPs is 3 times higher than that between spherical ones.[26,30] Hence, studying colloidal NCb superlattices will not only provide insight into the role of organic ligands in governing the self-assembly processes but also possibly result in the discovery of novel, tunable collective properties from the NCb ensembles.[23,31−36]

Herein we report the self-assembly of anisotropic Pt NCbs using a home-built evaporation-controlled system. With the assistance of transmission electron microscopy (TEM) tomographic analysis, we have identified solvent-dependent self-assembly of Pt NCb superlattices. In brief, Pt NCbs self-organized into a simple-cubic (*sc*) superstructure from aromatic toluene, whereas they self-assembled into a body-centered-tetragonal (*bct*) superstructure from aliphatic hexane. Both translational and orientational orderings were present in both the *sc* and *bct* superstructures. The construction of the square arrays of Pt NCbs within each layer is directly encoded in the cubic shape, and the variations in the superlattice symmetry are believed to be a direct result of delicate control over the ligand–solvent and ligand–ligand interactions during the heterogeneous-interface-induced self-assembly of colloidal Pt NCbs. Thus, our work has demonstrated the effectiveness of an easily accessible variable for expanding the available categories of self-assembly with nonspherical NPs as the building blocks.

■ RESULTS AND DISCUSSION

Precise control over NP shape, size distribution, and surface chemistry is essential to permit the rational assembly of NPs into ordered solids. In the studied system, Pt NCbs were prepared using a previously developed synthetic procedure[33] involving reduction of platinum(II) acetylacetonate in a mixture of oleic acid and oleylamine in the presence of hexacarbonyltungsten at an elevated temperature. The organic ligands coated on the resultant Pt NCbs play multiple roles during the synthesis of the Pt NCbs. First, they prefer to stabilize (100) crystallographic planes and promote growth in other directions when the Pt seeds initially nucleate from the precursors, resulting in the ultimate formation of (100)-enclosed Pt NCbs. Second, the covalent coordination of these aliphatic ligands onto the Pt NCbs allows them to be readily dissolved in a nonpolar or moderately polar solvent but reversibly aggregated in a strongly polar one. This feature can be utilized not only in the post-treatment size selection to obtain uniform NPs but also in the controlled two-solvent destabilization process to prepare ordered NP assemblies.[10,37] Lastly, the "shells" of soft ligands surrounding the "cores" of these hard Pt NCbs have the potential to direct the symmetry of the self-assembled pattern to a desired superstructure, especially when they are solvated in different media.

Figure 1a shows a typical TEM image of the as-prepared Pt NCbs, indicating that each of these NCbs is surrounded by four equivalent (100) planes in the monolayer with an average side length of 10.0 nm. As a result of the capping of organic ligands on the (100) surfaces of these NCbs, the average interparticle spacing observed was about 2.5 nm as determined from the TEM images. Since the length of either oleic acid or oleylamine is around 1.8 nm, the surface-to-surface spacing of adjacent NCbs should be ∼3.6 nm if these ligands contact each other in a tail-to-tail manner (i.e., if there is no intercalation section

dx.doi.org/10.1021/ja408250q | J. Am. Chem. Soc. 2014, 136, 1352−1359

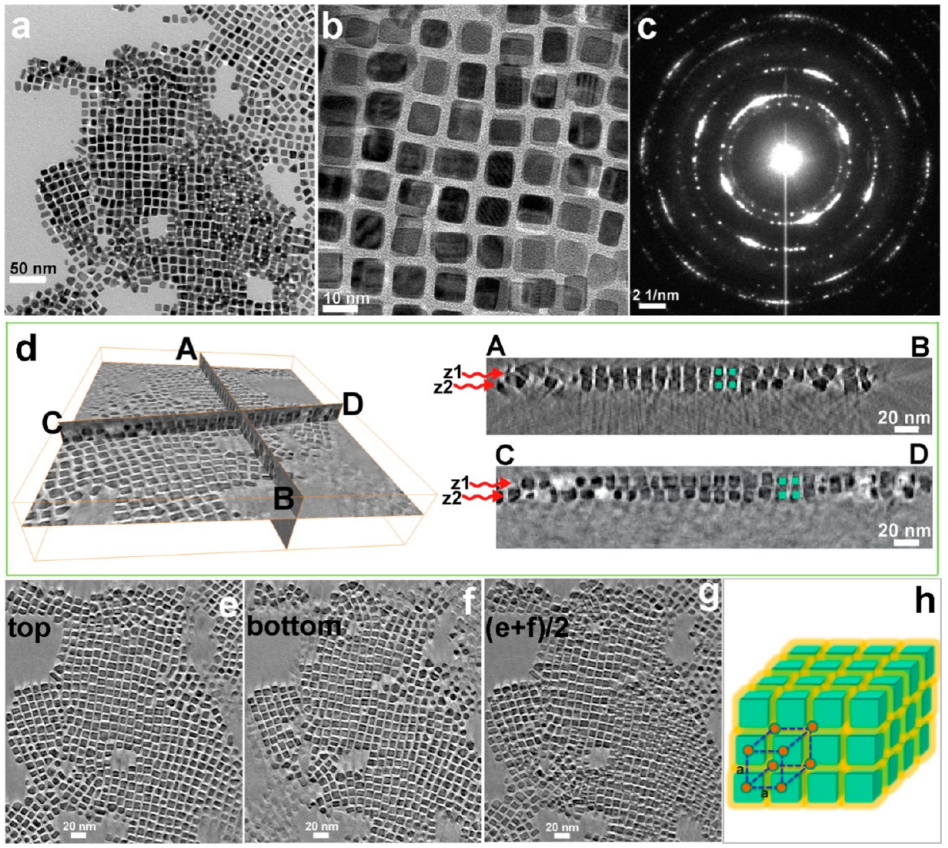

Figure 2. Self-assembly patterns of Pt NCbs generated from a toluene solvent. (a) TEM image. (b) Magnified image from (a) and (c) SAED pattern from the same area. (d) 3D reconstruction (left) with two orthogonal views AB and CD (right). (e, f) Slice views of the top and bottom layers at the heights of $z1$ and $z2$, respectively, as indicated in (d). (g) Calculated image obtained by averaging (e) and (f). (h) Structure model of the *sc* superstructure assembly.

between the ligands). The shorter interparticle spacing observed indicates that these Pt NCbs settled on a Cu grid facilitated a strong ligand–ligand interaction even without any assembly control. The side-view and top-view schemes of the home-built self-assembly setup are illustrated in Figure 1b,c, respectively. The purposes of this design are to reduce the kinetic effect during the assembly process by slowing down the solvent evaporation and to enable TEM observation of the as-formed superstructures on an electronically transparent Cu substrate. In this setup, the substrate is a two-layer combination: the bottom portion is a (111) surface-polished square Si wafer with dimensions of 15 mm × 15 mm, and the top layer consists of a 200 mesh Cu grid coated with a Formvar film and a "light" layer of carbon to protect the Formvar from the solvent. Because of the considerable surface tension of the Pt NCb colloidal suspensions on the Si wafer, the bottom Si wafer was intentionally designed to constrain Pt NCb suspensions without spreading out, while assemblies on the Cu grid were collected for TEM characterization. The concentrations of Pt NCbs in both hexane and toluene were adjusted to be ~0.1 M as the stock suspensions, resulting in the formation of assemblies with several layers of Pt NCbs. In a typical sample preparation, 20 μL of the stock dispersion was drop-cast onto the designed substrate, immediately covered with a weight dish (41 mm in length and 8 mm in height), and seamed with sealing tape. The use of this translucent dish not only "trapped" the solvent vapor in a closed environment to achieve controlled evaporation for NCb self-assembly but also enabled direct visualization of the physical changes associated with this self-assembly process, such as the variation of droplet height and the solvent drying progress. Because of the differences of the intrinsic physical properties of the solvents, such as density and saturated vapor pressure, it took about 1 h for hexane and 2 h for toluene to completely evaporate and afford solid superlattices of Pt NCbs. The presence of colorful spinodal decomposition morphologies instead of coffee-stain-like rings on these final assemblies prepared with either solvent was the first successful sign of achieving a long-range ordering in the Pt NCb patterns. This outcome could grow out of careful control over the solvent evaporation dynamics using the home-built system, which may potentially serve as a model setup for generating self-assembled superstructures with desired nano/mesoscale features and properties.

Figure 2 shows TEM tomographic results for Pt NCb superlattices assembled from aromatic toluene. The coexistence of monolayer and bilayer NCb assemblies in the selected area (Figure 2a) demonstrates unambiguously that Pt NCbs in both regions prefer to contact each other via their (100) faces and to have a square face-to-face conformation. It is also evident that these Pt NCbs sit on their flat (100) planes in the monolayer region. This behavior may be explained by the fact that a maximum interface contact between an NCb and the substrate will minimize its free energy. The case of these Pt NCbs is different from what we observed for octahedral Pt_3Ni or In_2O_3 NPs, as the latter could settle their (111) faces, (110) edges, or (100) vertices on the substrate depending on the preparation conditions.[33,38−40] In the magnified bilayer zone, the Pt NCbs on the top layer take the same orientation as the bottom ones

dx.doi.org/10.1021/ja408250q | J. Am. Chem. Soc. 2014, 136, 1352−1359

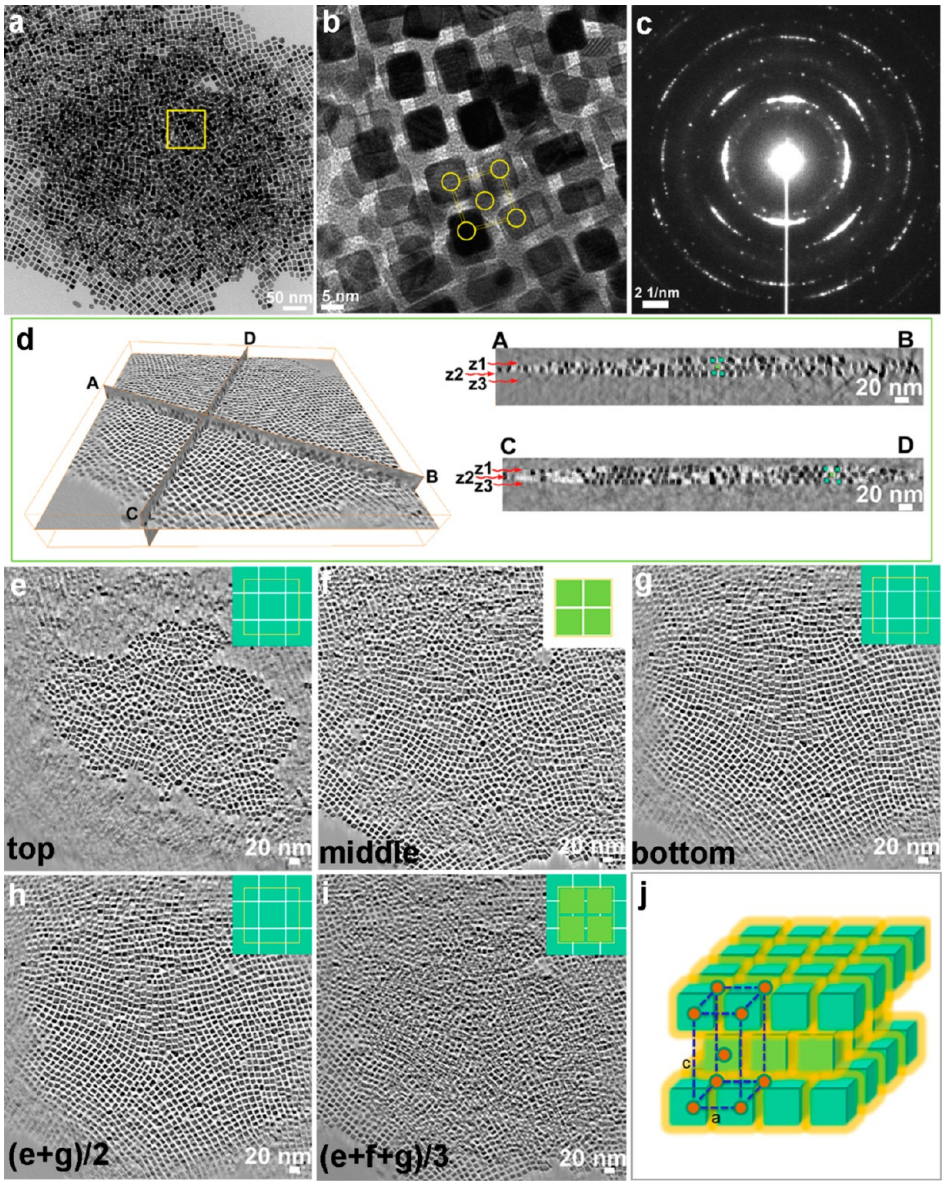

Figure 3. TEM and tomographic results of Pt NCb self-assembly generated from hexane as the solvent. (a) TEM image. (b) Magnified image and (c) SAED pattern of the framed area in (a). (d) 3D reconstruction (left) with two orthogonal views AB and CD (right). (e–g) Slice views of the top, middle, and bottom layers at the heights of $z1$, $z2$, and $z3$, respectively, as indicated in (d). (h, i) Images obtained as the average of (e) and (g) and average of (e), (f) and (g), respectively. Unit cells are outlined. (j) Structure model of the *bct* assembly.

with face-to-face contact between the two layers (Figure 2b). This conformation was confirmed by the selected-area electron diffraction (SAED) pattern on a double-layer assembly (Figure 2c), which shows that the four strongest diffraction spots originate from the (200) planes of the Pt NCbs, indicating a high degree of orientation coherence of the NCbs in their superlattice sites. In order to further locate each NCb in this bilayer superstructure, an electron tomography technique was used to obtain a detailed 3D mapping image, as shown in Figure 2d–g as well as video 1 in the Supporting Information. During the image-collection process, a beam of electrons was passed through the selected bilayer region at incremental degrees of rotation around the sample center.[23] Figure 2d illustrates a cross-sectional view of the 3D reconstructed volume (left) and two orthogonal cross-section views marked as AB and CD (right). It is clear that within this double-layer assembly, the Pt NCbs in the top layer ($z1$) from both slices are directly located on the top surface of the bottom layer ($z2$). The corresponding TEM images of the top and bottom layers as marked with the height labels $z1$ and $z2$, respectively, in Figure 2d and the calculated image obtained by averaging the images for the two layers are presented in Figure 2e–g, respectively. From the AB and CD lateral views shown in Figure 2d, the horizontal length was measured as 12.2 nm and the vertical height as 11.5 nm with an uncertainty of 5.7%. Considering the systematic error along the vertical direction produced in TEM tomography, it is reasonable to assume that this is a cubic structure. Therefore, the observation of almost identical positions of the NCbs in both layers enables us to construct a packing pattern of NCbs assembled from toluene as a primitive cubic or *sc* superstructure (space group $Pm\bar{3}m$, No. 221) with a lattice constant (a) of 12.2 nm and an average interparticle spacing of 2.23 ± 0.28 nm (Figure 2h).

dx.doi.org/10.1021/ja408250q | *J. Am. Chem. Soc.* 2014, 136, 1352–1359

Scheme 1. Schematic Illustration of the Formation of Pt NCb *sc* and *bct* Superstructures in the Presence of Toluene and Hexane Solvents, Respectively

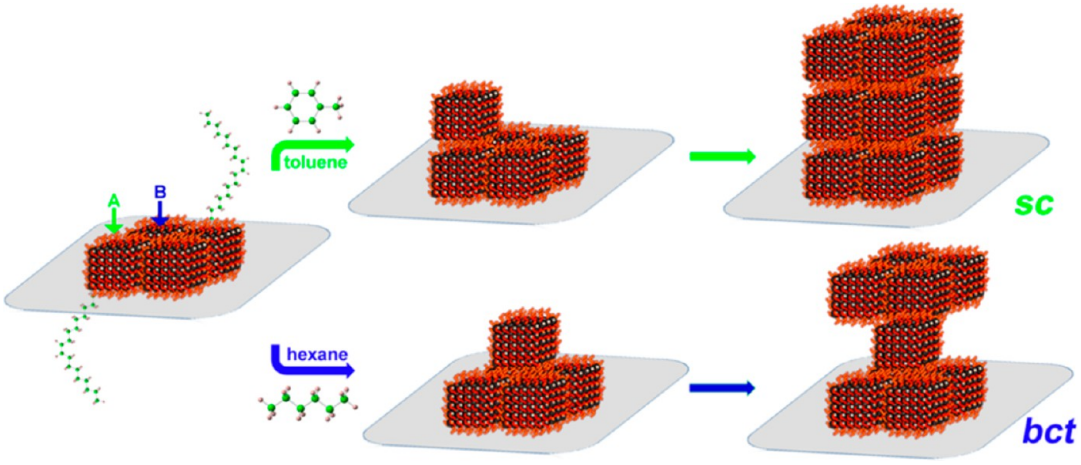

Within this *sc* superlattice, the (100) planes of an individual Pt NCb are coplanar with the (100) planes of the NCb superstructure, which are parallel or perpendicular to the substrate surface. Notably, although the *sc* superstructure was predicted to be the most stable assembly pattern for "naked" (or hard) cubes,[41] it has rarely been reported in other NCb systems.[32] Such behavior is probably due to the perturbations caused by the presence of outside soft ligands on these colloidal NCbs. On the other hand, the interactions of these soft ligands do provide an additional variable to enrich the types of self-assembled NP superstructures.

When the aromatic toluene solvent was replaced by aliphatic hexane while other conditions were kept the same, we accordingly obtained TEM patterns of Pt NCb assemblies as shown in Figure 3 and video 2 in the Supporting Information, which exhibit a significant change in the packed superstructure. The assembly region covered in Figure 3a includes various layers, from monolayer to bilayer to trilayer, as indicated by the different stacking-induced contrasts. Although the NCbs in the monolayer region still pack themselves in a way similar to that in the case of toluene, they display distinct assembly patterns in multilayer regions. To clearly probe the assembly structure in the multilayer regions, the part marked with a yellow square in Figure 3a was correspondingly magnified and is presented in Figure 3b, which shows the projection of NCbs from several layers. It appears that the NCbs in the top and bottom layers take the same positions as highlighted with four open circles at the corners, whereas those in the middle layer are placed in the interstices produced by the NCbs at the four corners in either the top or bottom layer.

This arrangement was confirmed by additional TEM tomographic patterns of bilayer NCb assembly, as shown in Figure S1 in the Supporting Information. Despite their seemingly distinct assembly symmetry compared with that of the previous *sc* superstructure, in both cases within each layer the Pt NCbs are assembled in the same manner, that is, square face-to-face orientations, as evidenced by the SAED pattern (Figure 3c). The corresponding 3D reconstructed volume and two delicately chosen cross sections are shown in Figure 3d. From these images, three different layers are easily recognized. The top and bottom layers share vertically equivalent positions, and the middle one is horizontally shifted along a certain distance relative to them. It can be clearly seen that the average distance between the top and bottom layers is much larger than the interparticle distance within the same layer. Figure 3e,f displays their related TEM images at the different heights labeled as $z1$, $z2$, and $z3$ as well as their relative in-plane coordinates (image insets). As is shown, the NCbs in the middle layer have different coordinates from those in the other two layers, which may be explained as a result of simultaneous in-plane movements by half of the interparticle distance along two horizontal directions. In addition, the superposition images of the bottom and top layers (Figure 3g) and all layers (Figure 3h) suggest a *bct* stacking pattern (space group $I4/mmm$, No. 139), in which $a = b = 12.5$ nm and $c = 20.0$ nm. Even though there is a systematic error associated with the vertical height measurement in TEM tomography, since the difference between the measured a (or b) and c values is much larger, the tetragonality of the observed superstructure is still valid. Specifically, if we assume that the error along the vertical direction is the same as that indicated in Figure 2 (within 5.7%), the lattice parameter c is in the range 20.0−21.1 nm. The interparticle spacing within the horizontal layers is determined to be 2.59 nm, which is 16% larger than that for the *sc* superlattice (2.23 nm).

It should be pointed out that the solvent-dependent superstructures comprising Pt NCbs are fully tenable. For a TEM tomography demonstration, we have to select areas with smaller size and fewer layers for simplicity. Although the TEM observation area is limited, we examined the superstructures at multiple sample locations in the large-scale territory on a grid in both the toluene and hexane cases. Some of the additional TEM and scanning transmission electron microscopy (STEM) images for both cases are presented in Figures S2−S5 in the Supporting Information. These observations further confirm that the *sc* and *bct* packing symmetries dominate the structures in toluene- and hexane-derived superlattices, respectively, and indicate that the structure selectivity and uniformity are high in each case.

As illustrated in Scheme 1, the final symmetry of the Pt NCb superlattice on a Cu grid could be tailored from *sc* to *bct* through variation of the dispersion medium only (from aromatic toluene to aliphatic hexane in this work). The delicate control over the superstructure of colloidal self-assembly may be attributed to the combination of their anisotropic cubic shapes and the presence of "soft" organic ligands outside "hard"

dx.doi.org/10.1021/ja408250q | *J. Am. Chem. Soc.* 2014, 136, 1352−1359

Pt NCbs. Because of the peculiar geometry of Pt NCbs, their square arrays are energetically favored by excluded-volume interactions, which could explain the exclusive tetracoordination of Pt NCbs within each layer regardless of the solvent characteristics. In the same way, the *sc* superstructure is expected to be the most stable structure for a 3D assembly. However, the presence of "soft" ligands can introduce perturbations during the self-assembly process, making certain deviations occur in the final Pt NCb superlattice symmetry.[32] In the studied system, Pt NCbs are coated with hydrophobic aliphatic chains, enabling the effective dissolution of these NPs into solvents such as hexane and toluene. Both solvents are considered as "good solvents" for Pt NCbs, as they can penetrate the ligand coronas all the way to the NCb surfaces.[42] Thus, the Pt NCbs remain well separated in these solvents, forming stable colloidal dispersions as nascent solutions. During the gradual evaporation of the solvent, however, the intrinsic differences of these two solvents could produce significant effects, especially when the interparticle spacing is less than twice the ligand length (3.6 nm). For example, aliphatic hexane consists of a straight hydrocarbon chain as a nonpolar solvent based on Hansen parameters, whereas aromatic toluene contains one aromatic ring with a slight polarity. According to Flory–Huggins theory,[43,44] these NCb-anchored aliphatic ligands could be relatively better solvated with aliphatic hexane than with aromatic toluene. In the case of toluene, adjacent Pt NCbs prefer to approach each other in a way to achieve the maximum ligand–ligand interactions rather than the energetically less favorable ligand–solvent interactions. Meanwhile, the effective thickness of the capping ligands around Pt NCbs might accordingly "shrink" and act like part of the hard cubes during the condensation process. Thus, the use of toluene as a dispersion medium leads to the final formation of the *sc* superstructure as the stable assembly pattern (top section in Scheme 1), in which ligands between proximate NCbs in all of the six equivalent directions can interdigitate maximally. In contrast to toluene, Pt NCbs that are well-solvated with hexane completely protrude their ligands into the solvent and behave more like spherical NPs. Therefore, the second layer of Pt NCbs would prefer to take the interstitial space created by four adjacent NCbs on the first layer with the lowest energy. Furthermore, the strong interactions between the ligands and hexane solvent result in a possible avoidance of ligand–ligand interactions. Hence, the reduced ligand passivation at NCb corners is another driving force for the second-layer Pt NCbs to occupy the first-layer interstitial space. Considering the geometry of 10.0 nm NCbs with 2.59 nm spacing between them, in the *sc* structure the face-to-face interaction area is 100%, while in the *bct* structure only 56.3% of the areas are faced to each other to minimize the ligand–ligand interactions. Compared to the toluene case, the increased interparticle spacing within each layer as described above further suggests a less intensive ligand–ligand interaction in the presence of hexane. Consequently, the *bct* superstructure from hexane is an energetically favorable assembly for Pt NCbs (bottom section in Scheme 1).

It should be noted that the shape of the building blocks can also impact the final superstructure and its formation driving force. Disch and co-workers[27,45] demonstrated a superstructural transition from *sc* to *bct* for slightly truncated iron oxide NCbs as the degree of the NCb truncation increased, and they attributed the *bct* formation to a minimization of the interparticle energy through symmetry breaking in the interparticle interactions. In the case of Pt NCbs, the building blocks, being "perfectly" sharp (no truncation) and much more densely packed along the *c* axis in comparison with the *a* axis, dictate the breaking of the cubic symmetry, resulting in a *bct* superstructure. Mechanistically, the *bct* packing seems to be stabilized by the larger horizontal surface-to-surface distance found in hexane-cast superlattices. In addition, the reduced ligand density at vertices may facilitate the reduced *c* spacing in the *bct* structure.[40] All of these factors appear to work in synergy to stabilize the observed tetragonal structure. As is known, any perturbation in an NC superlattice system can cause breaking of the ideal cubic symmetry. In our Pt NCb experiments, all other assembly factors except the solvent type were kept the same. Thus, the small fluctuations among the NCb interactions when toluene was replaced by hexane should be the only reason to cause the transition from the *sc* to the *bct* superstructure. Consequently, both the solvent type and NP morphology can be controlling factors for NP superlattice formation, though with different interaction mechanisms.

As an extension of our study, we utilized hexane-based Pt NCb suspensions and assembled them into large-area and multilayered supercrystals in a vial using a slow-evaporation approach as described previously.[32] As indicated in the scanning electron microscopy (SEM) image presented in Figure S6a in the Supporting Information, the supercrystal has a top-surface area of several hundred square micrometers and is thousands of layers in thickness. Figure S6b shows that the NCbs on the top surface of the supercrystal are well-aligned, which can be further illustrated as square arrays in the fast Fourier transform (FFT) pattern generated from Figure S6b, which is shown in Figure S6c. To determine the entire superstructure in bulk, this specimen was further analyzed using a synchrotron small-angle X-ray scattering (SAXS) technique.[46] As shown in the inset of Figure S6d, in which two of the orientation-induced strongest spots with apparent saturation were masked off for purposes of reasonable integration and subsequent structural refinement, the 2D SAXS pattern shows a typical spotty feature in the scattering rings, indicating excellent translational coherence and large domains of nucleated NCb supercrystals. The *d* spacings of individual peaks in the corresponding 1D plot of intensity versus peak position (2θ) (Table S1 in the Supporting Information) were subsequently fitted by a standard Le Bail refinement[47−49] using the GSAS package.[50] The results suggested a *bct* superstructure (space group $I4/mmm$) with lattice parameters of $a = b = 17.4$ nm and $c = 20.2$ nm. Further investigation of the assembly preparation and superstructure characterization of such large-area and multilayered supercrystals is still in progress. Although the preliminary data from this study cannot be used to directly support the TEM tomography observations in the case of hexane as the solvent because of the different substrates and possibly different assembly rates, which result in different values of the supercrystal lattice parameter *a* (17.4 nm from SAXS vs 12.5 nm from TEM), the hexane-based large-area assembly study still demonstrates a similar trend toward the formation of a *bct* superstructure.

■ CONCLUSIONS

By varying the interactions between the capping ligands and the self-assembly solvent by changing the solvent from aliphatic hexane to aromatic toluene, we have demonstrated two distinct Pt NCb assembled superstructures using a TEM tomographic technique. On copper TEM grids in the home-built setup, Pt

NCbs self-organized into a simple-cubic superstructure when cast from aromatic toluene, whereas they self-assembled into a body-centered-tetragonal superstructure when cast from aliphatic hexane. The insight into ligand−solvent interactions gained from this work represents a piece of new information that will further promote our understanding of the formation mechanisms in the self-assembly of nonspherical NPs. In addition, this work provides a new general procedure for the systematic design, preparation, and characterization of ordered structures of NPs for future device development and applications.

■ ASSOCIATED CONTENT

Supporting Information

Experimental section, TEM and tomographic images of the double-layer Pt NCb self-assembly generated from hexane, additional TEM images of Pt NCb superlattices self-assembled from toluene and hexane observed at different locations on the Cu grids, SEM images and SAXS patterns with Le Bail refinement fitting profile, and TEM tomography videos (AVI) of Pt NCb patterns generated from toluene and hexane. This material is available free of charge via the Internet at http://pubs.acs.org.

■ AUTHOR INFORMATION

Corresponding Authors

jfang@binghamton.edu
zluo@uncfsu.edu

Notes

The authors declare no competing financial interest.

■ ACKNOWLEDGMENTS

This work was partially supported by S^{3}IP at Binghamton University and the DOE STTR Program. Pt NCb self-assembly was prepared at the Cornell High Energy Synchrotron Source (CHESS). Z.Q. acknowledges the J. Robert Oppenheimer (JRO) Fellowship supported by the Laboratory-Directed Research and Development (LDRD) Program of Los Alamos National Laboratory, which is operated by Los Alamos National Security LLC under DOE Contract DE-AC52-06NA25396. CHESS is supported by the National Science Foundation and the National Institutes of Health/National Institute of General Medical Sciences under NSF Award DMR-0936384. We appreciate Welley Siu Loc from Pennsylvania State University for her assistance in the design and completion of Scheme 1.

■ REFERENCES

(1) Young, K. L.; Jones, M. R.; Zhang, J.; Macfarlane, R. J.; Esquivel-Sirvent, R.; Nap, R. J.; Wu, J.; Schatz, G. C.; Lee, B.; Mirkin, C. A. *Proc. Natl. Acad. Sci. U.S.A.* **2012**, *109*, 2240−2245.

(2) Black, C. T.; Murray, C. B.; Sandstrom, R. L.; Sun, S. *Science* **2000**, *290*, 1131−1134.

(3) Tao, A.; Sinsermsuksakul, P.; Yang, P. *Nat. Nanotechnol.* **2007**, *2*, 435−440.

(4) Urban, J. J.; Talapin, D. V.; Shevchenko, E. V.; Kagan, C. R.; Murray, C. B. *Nat. Mater.* **2007**, *6*, 115−121.

(5) Wang, T.; Zhuang, J.; Lynch, J.; Chen, O.; Wang, Z.; Wang, X.; LaMontagne, D.; Wu, H.; Wang, Z.; Cao, Y. C. *Science* **2012**, *338*, 358−363.

(6) Yin, Y.; Xia, Y. *J. Am. Chem. Soc.* **2003**, *125*, 2048−2049.

(7) Sun, S.; Murray, C. B.; Weller, D.; Folks, L.; Moser, A. *Science* **2000**, *287*, 1989−1992.

(8) Bishop, K. J. M.; Wilmer, C. E.; Soh, S.; Grzybowski, B. A. *Small* **2009**, *5*, 1600−1630.

(9) Min, Y.; Akbulut, M.; Kristiansen, K.; Golan, Y.; Israelachvili, J. *Nat. Mater.* **2008**, *7*, 527−538.

(10) Murray, C. B.; Kagan, C. R.; Bawendi, M. G. *Science* **1995**, *270*, 1335−1338.

(11) Sun, Z.; Luo, Z.; Fang, J. *ACS Nano* **2010**, *4*, 1821−1828.

(12) Talapin, D. V.; Murray, C. B. *Science* **2005**, *310*, 86−89.

(13) Evers, W. H.; Friedrich, H.; Filion, L.; Dijkstra, M.; Vanmaekelbergh, D. *Angew. Chem., Int. Ed.* **2009**, *48*, 9655−9657.

(14) Vanmaekelbergh, D. *Nano Today* **2011**, *6*, 419−437.

(15) Yin, Y.; Alivisatos, A. P. *Nature* **2005**, *437*, 664−670.

(16) Choi, J. J.; Bealing, C. R.; Bian, K.; Hughes, K. J.; Zhang, W.; Smilgies, D.-M.; Hennig, R. G.; Engstrom, J. R.; Hanrath, T. *J. Am. Chem. Soc.* **2011**, *133*, 3131−3138.

(17) Nie, Z.; Fava, D.; Kumacheva, E.; Zou, S.; Walker, G. C.; Rubinstein, M. *Nat. Mater.* **2007**, *6*, 609−614.

(18) Wang, Z.; Schliehe, C.; Bian, K.; Dale, D.; Bassett, W. A.; Hanrath, T.; Klinke, C.; Weller, H. *Nano Lett.* **2013**, *13*, 1303−1311.

(19) Whetten, R. L.; Shafigullin, M. N.; Khoury, J. T.; Schaaff, T. G.; Vezmar, I.; Alvarez, M. M.; Wilkinson, A. *Acc. Chem. Res.* **1999**, *32*, 397−406.

(20) Zhang, Y.; Lu, F.; van der Lelie, D.; Gang, O. *Phys. Rev. Lett.* **2011**, *107*, No. 135701.

(21) Korgel, B. A.; Fitzmaurice, D. *Phys. Rev. B* **1999**, *59*, 14191−14201.

(22) Park, S. Y.; Lytton-Jean, A. K. R.; Lee, B.; Weigand, S.; Schatz, G. C.; Mirkin, C. A. *Nature* **2008**, *451*, 553−556.

(23) Quan, Z.; Fang, J. *Nano Today* **2010**, *5*, 390−411.

(24) Ahniyaz, A.; Sakamoto, Y.; Bergström, L. *Proc. Natl. Acad. Sci. U.S.A.* **2007**, *104*, 17570−17574.

(25) Chan, H.; Demortière, A.; Vukovic, L.; Král, P.; Petit, C. *ACS Nano* **2012**, *6*, 4203−4213.

(26) Choi, J. J.; Bian, K.; Baumgardner, W. J.; Smilgies, D.-M.; Hanrath, T. *Nano Lett.* **2012**, *12*, 4791−4798.

(27) Disch, S.; Wetterskog, E.; Hermann, R. P.; Salazar-Alvarez, G.; Busch, P.; Brückel, T.; Bergström, L.; Kamali, S. *Nano Lett.* **2011**, *11*, 1651−1656.

(28) Rycenga, M.; McLellan, J. M.; Xia, Y. *Adv. Mater.* **2008**, *20*, 2416−2420.

(29) Lapointe, C. P.; Mason, T. G.; Smalyukh, I. I. *Science* **2009**, *326*, 1083−1086.

(30) Liljeroth, P.; Overgaag, K.; Urbieta, A.; Grandidier, B.; Hickey, S. G.; Vanmaekelbergh, D. *Phys. Rev. Lett.* **2006**, *97*, No. 096803.

(31) Quan, Z.; Luo, Z.; Loc, W. S.; Zhang, J.; Wang, Y.; Yang, K.; Porter, N.; Lin, J.; Wang, H.; Fang, J. *J. Am. Chem. Soc.* **2011**, *133*, 17590−17593.

(32) Quan, Z.; Loc, W. S.; Lin, C.; Luo, Z.; Yang, K.; Wang, Y.; Wang, H.; Wang, Z.; Fang, J. *Nano Lett.* **2012**, *12*, 4409−4413.

(33) Zhang, J.; Fang, J. *J. Am. Chem. Soc.* **2009**, *131*, 18543−18547.

(34) Zhang, J.; Yang, H.; Yang, K.; Fang, J.; Zou, S.; Luo, Z.; Wang, H.; Bae, I.-T.; Jung, D. Y. *Adv. Funct. Mater.* **2010**, *20*, 3727−3733.

(35) Henzie, J.; Grünwald, M.; Widmer-Cooper, A.; Geissler, P. L.; Yang, P. *Nat. Mater.* **2012**, *11*, 131−137.

(36) Gong, J.; Li, G.; Tang, Z. *Nano Today* **2012**, *7*, 564−585.

(37) Murray, C. B.; Kagan, C. R.; Bawendi, M. G. *Annu. Rev. Mater. Sci.* **2000**, *30*, 545−610.

(38) Lu, W.; Liu, Q.; Sun, Z.; He, J.; Ezeolu, C.; Fang, J. *J. Am. Chem. Soc.* **2008**, *130*, 6983−6991.

(39) Zhang, J.; Luo, Z.; Martens, B.; Quan, Z.; Kumbhar, A.; Porter, N.; Wang, Y.; Smilgies, D.-M.; Fang, J. *J. Am. Chem. Soc.* **2012**, *134*, 14043−14049.

(40) Zhang, J.; Luo, Z.; Quan, Z.; Wang, Y.; Kumbhar, A.; Smilgies, D.-M.; Fang, J. *Nano Lett.* **2011**, *11*, 2912−2918.

(41) Damasceno, P. F.; Engel, M.; Glotzer, S. C. *Science* **2012**, *337*, 453−457.

(42) Kaushik, A. P.; Clancy, P. *J. Comput. Chem.* **2013**, *34*, 523−532.

(43) Flory, P. J. *J. Chem. Phys.* **1941**, *9*, 660.

(44) Huggins, M. L. *J. Chem. Phys.* **1941**, *9*, 440.

(45) Disch, S.; Wetterskog, E.; Hermann, R. P.; Korolkov, D.; Busch, P.; Boesecke, P.; Lyon, O.; Vainio, U.; Salazar-Alvarez, G.; Bergstrom, L.; Bruckel, T. *Nanoscale* **2013**, *5*, 3969−3975.
(46) Wang, Z.; Chen, O.; Cao, C. Y.; Finkelstein, K.; Smilgies, D.-M.; Lu, X.; Bassett, W. A. *Rev. Sci. Instrum.* **2010**, *81*, No. 093902.
(47) http://sdpd.univ-lemans.fr/iniref/lbm-story/.
(48) Le Bail, A.; Duroy, H.; Fourquet, J. L. *Mater. Res. Bull.* **1988**, *23*, 447−452.
(49) Le Bail, A. *Powder Diffr.* **2005**, *20*, 316−326.
(50) Larson, A. C.; Von Dreele, R. B. *General Structure Analysis System (GSAS)*; Los Alamos National Laboratory Report LAUR 86-748; Los Alamos National Laboratory: Los Alamos, NM, 2004.